

## Article

# Experimental Study on Seismic Performance of Prefabricated Columns Connected Using a Novel Dry Sleeve

Xiaoyi Hu <sup>1</sup>, Baojun Zhao <sup>2</sup>, Hao Wu <sup>1,\*</sup> , Abderrahim Djerrad <sup>1</sup>  and Dekai Zhang <sup>1,3</sup>

<sup>1</sup> College of Civil Engineering, Tongji University, 1239 Siping Rd., Shanghai 200092, China; 91118@tongji.edu.cn (X.H.); djerradabderahim@gmail.com (A.D.)

<sup>2</sup> China State Construction Hailong Technology Co., Ltd., Shenzhen 518017, China; zhaobj@cohl.com

<sup>3</sup> China Construction Eighth Engineering Division Corp., Ltd., Shanghai 200112, China

\* Correspondence: 2009wuhao\_tom@tongji.edu.cn

**Abstract:** Prefabricated structures are widely used because of their advantages of energy savings, environmental protection, standardization, and universality. However, due to the complex structure of the joints, it is easy to make the joint installation difficult and the prefabricated column connection unreliable, and further lead to the poor seismic performance of the structure. Therefore, a new type of dry sleeve joint with double screw sleeve without support is proposed, and the seismic performance and influencing factors of the new dry-sleeve-joint prefabricated column are studied. This study encompasses seven reinforced concrete columns characterized by cross-sectional dimensions of 600 mm × 600 mm. Among these, five specimens feature a novel dry sleeve connection, while the remaining two specimens were entirely cast-in-place. Low-cycle reversed loading experiments were conducted on all specimens to analyze and compare the damage patterns, hysteresis curves, skeleton curves, displacement ductility, energy dissipation capacity, and ultimate bearing capacity between precast and cast-in-place columns. Several parameters, including fabrication method, axial compression ratio, longitudinal reinforcement diameter, and hoop spacing, were examined. The findings demonstrated that the calculated-to-tested ratio of the ultimate bearing capacity for the prefabricated specimens was determined to be 0.62, indicating a high level of safety. The displacement ductility coefficient for each specimen ranged from 2.43 to 3.31, while the ultimate drift ratio was within the range of 1/41 to 1/33, satisfying the specified requirements for seismic performance. However, the hysteresis curve of the prefabricated specimens exhibited a pinching effect, which may be related to the existence of a weak layer on the joint surface of the post-cast section. In general, the shape of the new dry sleeve is maintained in the test, the connection form can effectively transfer the force, and the longitudinal bars can be strained and yield when the prefabricated column reaches the peak load. The new type of dry sleeve connection can be used for longitudinal reinforcement connection of reinforced concrete columns with seismic design.

**Keywords:** precast concrete column; dry sleeve connection; cyclic reversed loading experiment; seismic performance



**Citation:** Hu, X.; Zhao, B.; Wu, H.; Djerrad, A.; Zhang, D. Experimental Study on Seismic Performance of Prefabricated Columns Connected Using a Novel Dry Sleeve. *Buildings* **2024**, *14*, 249. <https://doi.org/10.3390/buildings14010249>

Academic Editor: Daniele Perrone

Received: 4 December 2023

Revised: 7 January 2024

Accepted: 12 January 2024

Published: 16 January 2024



**Copyright:** © 2024 by the authors. Licensee MDPI, Basel, Switzerland. This article is an open access article distributed under the terms and conditions of the Creative Commons Attribution (CC BY) license (<https://creativecommons.org/licenses/by/4.0/>).

## 1. Introduction

Since the issuance of “Several Opinions on Further Strengthening the Management of Urban Planning and Construction” by the Chinese State Council in 2016, the development of prefabricated buildings in China has ascended to the status of a national development strategy. One of the important ideas to improve the standard of urban construction is to encourage construction enterprises to develop new forms of construction and improve the capacity of prefabricated construction.

Prefabricated constructions have many advantages over traditional constructions. Liu [1] expounds the view that prefabricated buildings can effectively help realize the industrialization of construction projects and thus reduce the energy consumption of construction sites. In the past 10 years, the research on prefabricated concrete structures has

been intensified, and much of the experimentation, modeling, and theoretical research has been done on precast concrete structure components (precast composite column) [2–4], material properties [5–7], structural vibration behaviors [8,9], node connections [10–12], construction method [13,14], or other points of prefabricated modular buildings. Ou [2] compared the seismic performance difference between an ultra-high-performance concrete (UHPC) prefabricated pipe concrete composite column and a conventional reinforced concrete column (RC column), and found that the stiffness, yield load, and ductility performance of the UHPC prefabricated composite column were better than those of the RC column in quasi-static tests. Ahmed [5] conducted a feasibility assessment of mass timber as a mainstream building material in prefabricated construction, attributing the main benefits to the low labor in the construction process, aesthetic appeal, and prefabricated characteristics of timber panels. A near-surface-mounted fiber-reinforced polymer pile-splice system has been studied in Dolati's research [7] for prestressed precast concrete piles. Sun [11] proposed a new prefabricated beam–column node using a mechanical connection, which improved the seismic performance of prefabricated columns compared with sleeve-grouted-node specimens during the quasi-static test. Chourasia et al. [15] reviewed the modular structural system, modular node connection, design criteria and seismic performance, and proposed that node connection is the most important thing in modular buildings. It is pointed out that the extensive application of prefabricated modular buildings is hindered by the understanding of connections, the lack of design guidelines, the lack of experimental investigation of prefabricated modular buildings, and the limitations of transportation and treatment. At present, the joints of prefabricated specimens are usually connected in two ways: one is a wet connection using a grouting sleeve, and the other is a dry connection using a cold extrusion sleeve.

Regarding the overall seismic performance of the structure, experimental studies on precast columns with grouted sleeve connections have been conducted and documented in the literature [16–22]. Ong [16] conducted an experimental study on the prefabricated column connected by a grout-filled splice sleeve integrated with a shear key, and compared the mechanical performance with that of the cast-in-place column, and found that the bearing capacity and energy dissipation capacity of the two columns were basically the same. Similar test results can also be shown in the prefabricated concrete column with a proprietary grout-filled mechanical reinforcement splice (NMB splice) sleeve designed by Ogura [17] and the confined concrete column with horizontal strengthened bars spliced by grout sleeves designed by Zhang et al. [18]. Ameli et al. [19] studied the response of half-scale bridge column-to-cap beam assemblies under cyclic quasi-static load, and showed the result that the grouted splice sleeve connectors in the cap beam can be used in moderate to high seismic regions. Zhang [20] designed a quasi-static low-cycle reciprocating loading test of the vertical connection of the prefabricated assembled column with the sleeve grouting node, and determined the law of the seismic performance of the prefabricated column with the axial compression ratio and the strength of the grouting material. Findings from these studies indicated that the bearing and energy dissipation capacities of grouted sleeve precast (GSP) columns were similar to those of cast-in-place (CIP) columns. However, Kim [21] studied the seismic performance of precast columns connected by grout sleeves, and found that the connection position was the main failure location, and that the concrete near the sleeves fell off seriously and the stiffness was poor. In Riva's research [22], the bond failure at the grouted layer governed the failure mode in GSP columns, resulting in distinct hysteresis curves with a notable pinching effect and inferior energy dissipation capacity compared with CIP columns. In addition, the local performance of the sleeve and the grouting defects have a great influence on the failure mode of the sleeve. According to the results of Li's research [23], when the grouting defect length was short, the reinforcement tended to be pulled out of the joint; as the grouting defect length increased, the failure mode changed to the stripping failure between the reinforcement and grout or the scraping-plough-type pull-out failure of the reinforcement. As a result, the wet connection with grouting sleeves could be affected by grouting defects,

the performance of the sleeve connection could be unstable, and detecting grouting defects remained a prevalent challenge.

On the other hand, dry connections using cold extruded sleeves, regarding the overall seismic performance of the structure, were examined in Zhang [24] and Chen et al. [25]'s research. Results from these studies demonstrated that the energy dissipation capacity of precast columns with cold extruded sleeves was comparable to that of CIP columns. However, in terms of local sleeve performance, Zhang [24] reported instances of vertical or transverse cracks in some corner sleeves after reaching peak loads, thereby affecting specimen seismic performance.

In summary, it can be observed that the wet connection performance of the widely used grouting sleeve is plagued by grouting defects. Although the construction quality control method can reduce the probability of defects, it is still challenging to conduct relevant tests. The dry connection using the cold extrusion sleeve is susceptible to sleeve cracking and it is difficult to intervene by means of pre-test construction quality control. Hence, there is an urgent market need for a novel sleeve type that addresses these issues. In this paper, a new dry sleeve connection method for longitudinal steel bar connection of reinforced concrete column is proposed. The positioning and connection of steel bars at the joint is completed by matching the screw sleeve with the connecting sleeve, and the vertical alignment of the butt joint is adjusted by adjusting the length of the screw sleeve embedded in the connecting sleeve. The quasi-static tests of five precast reinforced concrete columns and two cast-in-place reinforced concrete columns are designed and carried out. The seismic performance and influencing factors of the precast columns with novel dry sleeve connection are researched, which provides the test basis for the application of the novel dry sleeve connection to prefabricated structures.

## 2. Test Overview

### 2.1. Specimens Design

The novel dry sleeve employed in this examination was supplied by Shanghai Hongse-lect Construction Technology Development Co., Ltd. (Shanghai, China), and the details are illustrated in Figure 1. Compared with the conventional grouting sleeve, the sleeve offers a significant advantage of saving time by eliminating the need for additional support during the construction process. During the construction process, the positioning and connection of the reinforcement at the node are completed by the cooperation of the screw sleeve and the connecting sleeve. Importantly, the vertical alignment of the butt joint is achieved by adjusting the length of the screw sleeve embedded in the connecting sleeve, thus removing the requirement for lateral support and optimizing construction time efficiency. The novel dry sleeve also has three features: (1) Improve construction efficiency: the pitch of all threads of the new type of executive sleeve joint is the same, which can improve the connection speed. (2) High fault tolerance rate: the axial deviation range of the connected steel bar is 0–35 mm; the horizontal deviation range is 0–15 mm. (3) Excellent performance: due to the HRB630 steel bar connection, the sleeve grade can reach 1 level joint performance indicators. The relevant sleeve has been entrusted to Shanghai Jianke Inspection Co., Ltd., and the outcomes of these inspections uniformly meet the requisite standards.

The experimental investigation consists of seven specimens of reinforced concrete columns, including five precast assembled columns with the novel dry sleeve connection method denoted as PC1~PC5, and two conventionally CIP-reinforced concrete columns denoted as CC1~CC2. Five distinct parameters were studied as detailed in Table 1, including the axial load ratio, longitudinal reinforcement diameter, hoop spacing, hoop position, and fabrication method. Figure 2 illustrates the geometric characteristics and specific reinforcement of the specimens. All specimens had an inverted T-shape, consisting of a column and a base. The column had cross-sectional dimensions of 600 mm × 600 mm, and a height of 2600 mm, while the base had cross-sectional dimensions of 1000 mm × 800 mm, and a length of 2200 mm. Longitudinal reinforcement consisted of 12 bars of diameter 20 mm ( $\rho = 1.12\%$ ) for all specimens, except PC3 and PC4, which were reinforced with

12 bars of diameter 25 mm ( $\rho = 1.75\%$ ). All specimens had hoop (transverse) reinforcement of 10@100 mm, except for specimen PC4, which had a diameter 10@150 mm. Specimen PC5 had the same parameters as specimen PC1, with the exception that the first hoop was not located at the base, serving to assess the pinning effect of the prefabricated column. For the construction joints, the effect of the shear force carried by the reinforcement is called the dowel action of the reinforcement [26]. CIP specimens (CC1~CC2) are cast as one piece, whereas precast specimens (PC1~PC5) involve separate casting of the base and column, followed by a two-stage assembly process: (1) installation of the dry sleeves; and (2) casting the lower part of the column (post-cast region). The post-cast region heights for specimens with longitudinal reinforcement of diameters 20 mm and 25 mm were 200 mm and 225 mm, respectively. Additionally, reinforced concrete legs with cross-sectional dimensions of 300 mm  $\times$  300 mm were provided at the lower end of the column body, equal in height to the post-cast region of each precast specimen. The legs were reinforced with longitudinal bars of 18 mm diameter and hoop reinforcement of 10@100 mm within the leg. Figure 3 illustrates the fabrication process of the specimens. The dry sleeve had a hexagonal shape, as presented in Figure 3. For the longitudinal reinforcement with diameters of 20 mm and 25 mm, the outer diameter of the sleeve was 40 mm and 47 mm on the opposite sides, the opposite corners were 41 mm and 48 mm. The sleeve lengths were 136 mm and 152 mm, and the total lengths of the longitudinal reinforcement inserted into the sleeve were 126 mm and 142 mm, respectively. Concrete of grade C30 was employed for both CIP specimens and precast specimens, and HRB400 was the reinforcement grade for both longitudinal and transverse reinforcement in all specimens. The measured mechanical properties of both concrete and reinforcement are summarized in Tables 2 and 3, respectively.

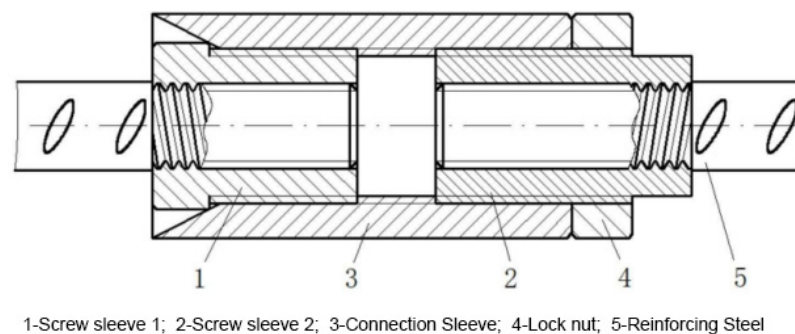


**Figure 1.** Detail view of the novel dry sleeve.

**Table 1.** Design parameters of specimens.

Specimen Number	n	$f_c$ (MPa)	$f_{c,m}$ (MPa)	N (kN)	Diameter of Reinforcing Steel (mm)	Reinforcement Ratio $\rho$ (%)	Hoop Reinforcement	Mating Hoop Characteristic Value $\lambda_v$
PC1	0.25	14.58	22.75	2047.41	20	1.12	$\phi 10@100$	0.25
PC2	0.4	14.26	22.62	3257.66	20	1.12	$\phi 10@100$	0.25
PC3	0.4	13.50	21.56	3105.18	25	1.75	$\phi 10@100$	0.26
PC4	0.4	14.43	23.47	3378.96	25	1.75	$\phi 10@150$	0.16
PC5	0.25	14.89	23.34	2101.02	20	1.12	$\phi 10@100$	0.26
CC1	0.25	13.50	21.56	1940.74	20	1.12	$\phi 10@100$	0.24
CC2	0.4	14.43	23.47	3378.96	20	1.12	$\phi 10@100$	0.24

Note: (1) n is the test axial pressure ratio,  $n = N/(f_{c,m}A)$ ,  $f_c$  and  $f_{c,m}$  are the design value of axial compressive strength of concrete and the average value of axial compressive strength of concrete, respectively. A is the cross-sectional area of the specimen column. For frame columns, the design axial pressure ratio is about 2 times the test axial pressure ratio [27]. (2) N is the axial pressure applied to the top of the column by the test. (3)  $\lambda_v$  is the design characteristic value of the matching hoop,  $\lambda_v = \rho_v f_{yv} / f_{c,m}$ ,  $\rho_v$  is the hoop volume, and  $f_{yv}$  is the measured hoop yield strength.



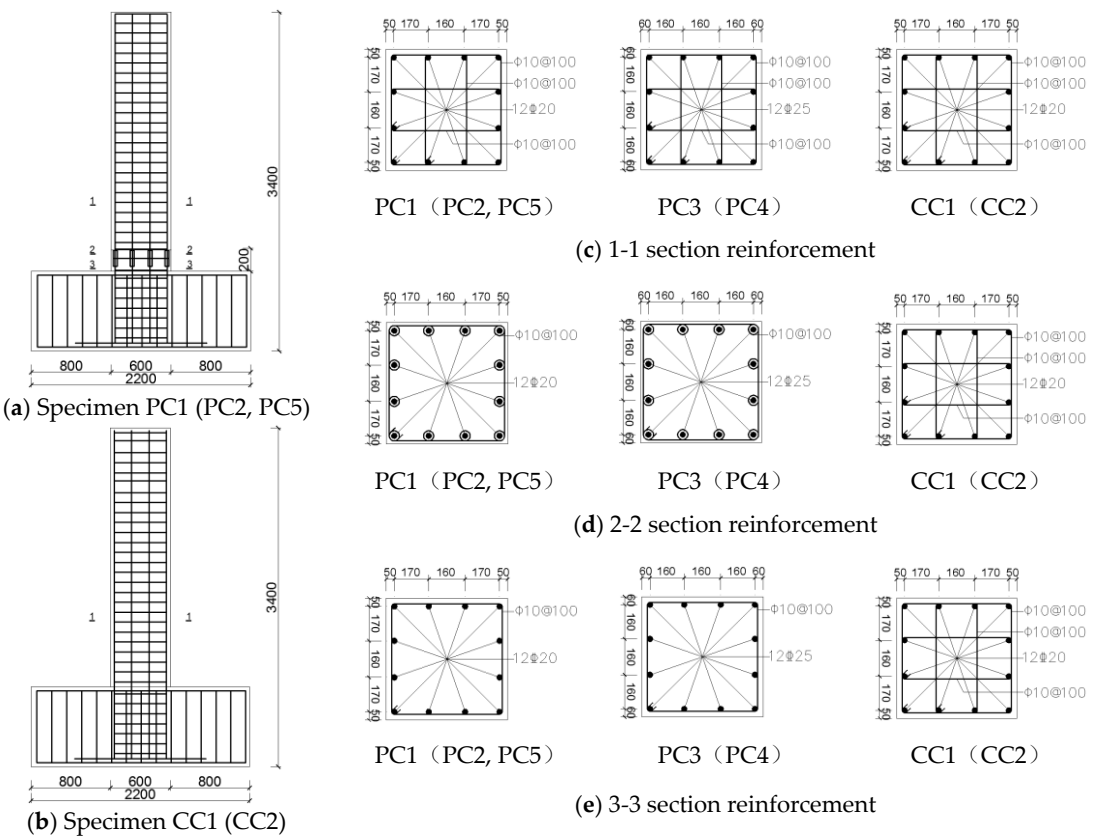


Figure 2. Dimensions and reinforcement details of specimens.

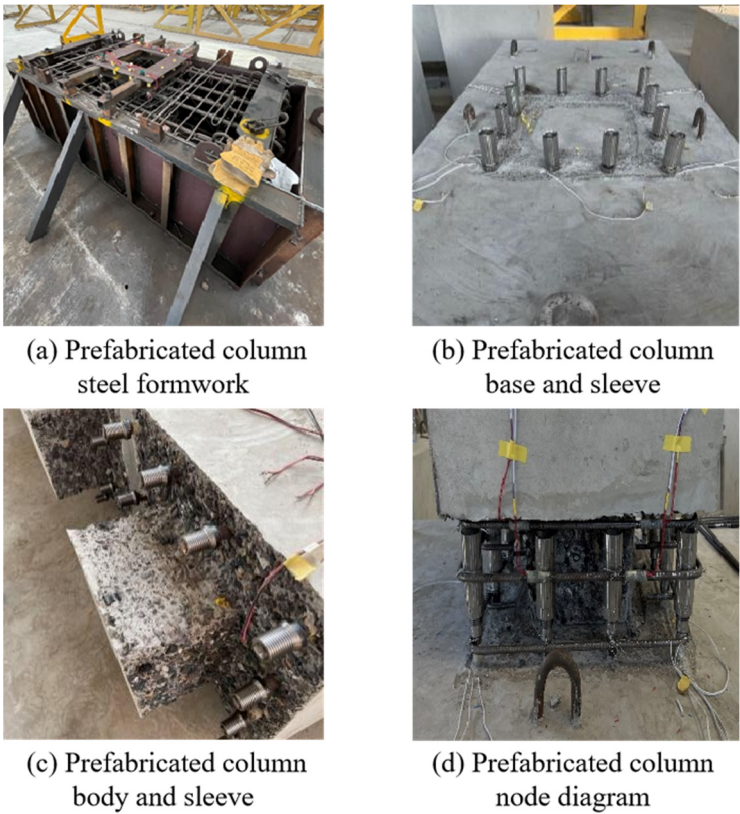


Figure 3. Fabrication of specimens.

**Table 2.** Measured mechanical properties of concrete.

Specimen Number	Specimen Parts	$f_{cu,m}$ (MPa)	$f_{cu,k}$ (MPa)	$f_{c,m}$ (MPa)	$f_c$ (MPa)
PC1	①	29.93	26.77	22.75	14.58
	②	52.69	45.86	40.05	24.90
PC2	①	29.77	26.28	22.62	14.26
	②	51.05	44.76	38.80	24.30
PC3	①	28.37	24.97	21.56	13.50
	②	44.94	39.03	34.16	21.19
PC4	①	30.88	28.57	23.47	14.43
	②	45.44	39.71	34.54	21.56
PC5	①	30.72	27.26	23.34	14.89
	②	54.95	47.53	41.77	25.80
CC1	①	28.37	24.97	21.56	13.50
CC2	①	30.88	28.57	23.47	14.43

Note: (1) The test parts in the table: ① refers to the specimen column body and base, ② refers to the location of the post-cast region. (2)  $f_{cu,k}$  is the standard value of concrete cubic compressive strength,  $f_{cu,k} = f_{cu,m}(1 - 1.645\delta)$ . The coefficient of variation was  $\delta = 0.04 \sim 0.09$ . The coefficient of variation was large due to the discrete data, resulting in the actual concrete strength grade of the base of the column body of the specimen was slightly lower than the design requirement, while the actual concrete strength of the post-cast region was generally at least one grade higher than the design requirement.  $f_{c,m}$  and  $f_c$  are the mean and design values of the axial compressive strength of concrete, respectively, where  $f_{c,m} = 0.76f_{cu,m}$ ; and  $f_c$  was taken equal to  $f_{cu,k}$  by GB50010-2010 “Concrete Structure Design Code” [28] (hereinafter referred to as “Mixing Code”).

**Table 3.** Measured mechanical properties of the reinforcement.

Diameter of Reinforcing Steel (mm)	$f_y$ (MPa)	$f_u$ (MPa)	$\epsilon_y(10^{-3})$
10	480	685	2.398
18	456	634	2.269
20	461	633	2.305
25	444	632	2.220

Note:  $\epsilon_y$  is the yield strain of the steel bar,  $\epsilon_y = f_y/E_s$ , where the modulus of elasticity was taken as GB50010-2010  $E_s = 2.0 \times 10^5$  MPa. The reinforcement with a diameter of 10 mm was used for the hoops, 18 mm for the column legs, and 20 mm and 25 mm for the column body longitudinal reinforcement.

Specimen processing was conducted at CCBI Anhui Hailong Construction Industry Co., Ltd., with monolithic specimens directly poured in Anhui Hailong, and prefabricated assembled specimens connected with the base by a specialized installation team in Anhui Hailong subsequent to mold release.

## 2.2. Test Setup and Instrumentation

Cantilever loading was used in the experimental setup, as shown in Figure 4. The base was securely affixed to the test bench using four screws with a diameter of 75 mm, along with lateral jacks. Horizontal loading was applied by a 100-ton horizontal actuator, while vertical loading was applied to the top of the column using a 400-ton jack featuring with a free-sliding servo plate. The vertical distance from the loading point to the bottom surface of the column measured 2230 mm. The vertical axial load was initially applied to the specimen and maintained at a constant level throughout the test. Subsequently, cyclic horizontal force was applied, initiating with forward loading and followed by tension reverse loading.

The experimental procedure adopted displacement control loading, with the loading protocol presented in Figure 5. Prior to yielding of the reinforcement bars, the displacement increment was set at 2 mm, and each level of the loading cycle at one time. Post-yielding, the displacement increment was increased to 5 mm, and each level of the loading cycle was repeated three times. The loading was stopped when the specimen bearing capacity dropped to 0.85  $P_u$ , where  $P_u$  represents the maximum test value for specimen bearing capacity.

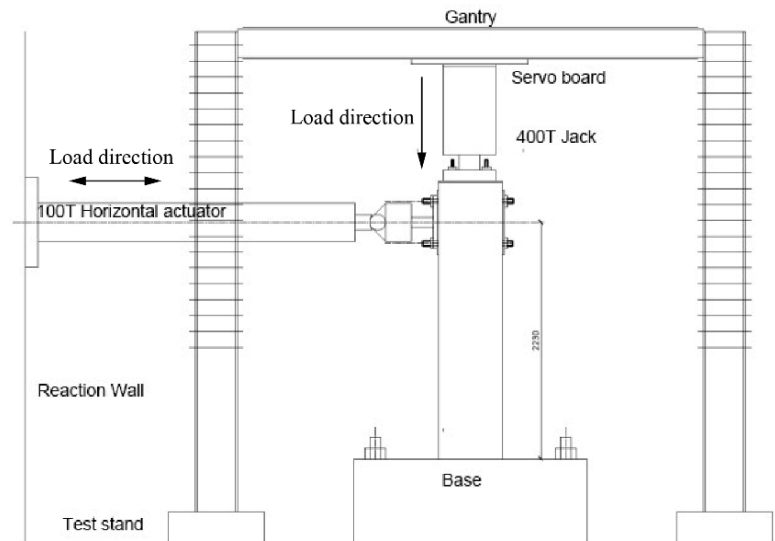


Figure 4. Sketch of test setup.

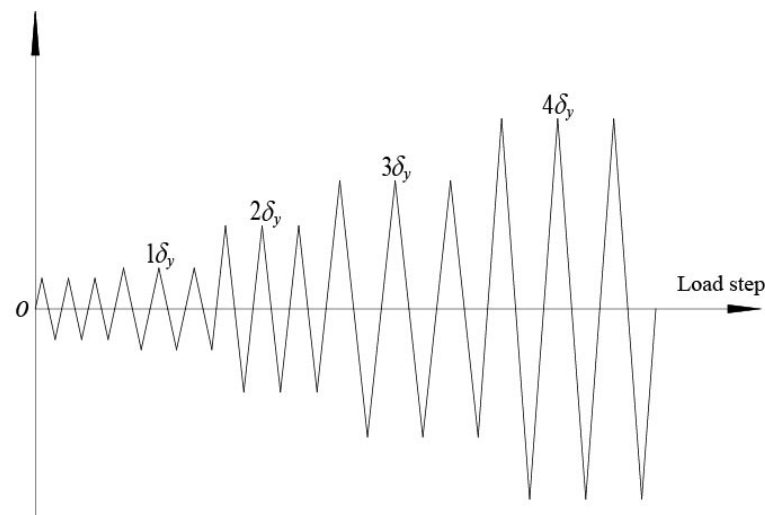
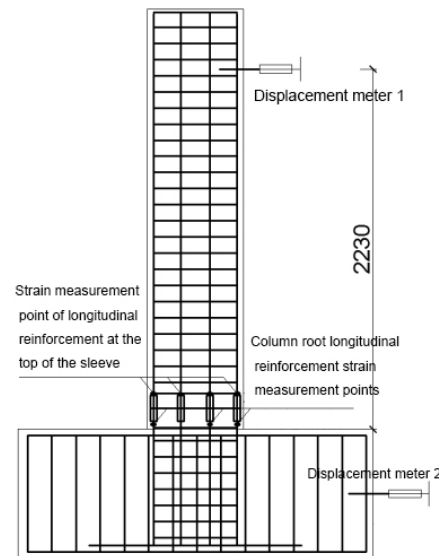


Figure 5. Loading protocol.

Horizontal displacement was measured using two sets of linear variable displacement transducers (LVDTs). The first set was arranged at the top of the column, precisely at the load position, while the other set was arranged at the mid-height of the base to measure the relative horizontal displacement between the top of the column and the base. The longitudinal strain of the sleeves was measured using 6 mm electrical strain gauges. These strain gauges were positioned at the bottom and top of the sleeve, specifically at 10 mm from the bottom and 10 mm from the top. Figure 6 presents the arrangement of LVDTs and strain gauges.



**Figure 6.** Measuring point arrangement.

### 3. Test Result and Failure Characteristics

#### 3.1. Specimens PC1~PC5

The crack pattern for all specimens as well as typical failure features are presented in Figures 7 and 8, respectively. Following the axial loading phase, cracks were initiated at the post-cast region, primarily consisting of annular horizontal cracks near the upper surface of the post-cast region and longitudinal cracks around the upper joint surface. These cracks seemed to be associated with the construction process. Upon subsequent application of horizontal loading, the following observations were made: Upon reaching a horizontal displacement of 10~15 mm at the top of the columns, a progressive yielding of the longitudinal reinforcement at the base of the column was observed. Horizontal annular cracks manifested at the upper joint surface, and the initiation of longitudinal and oblique cracks became apparent, primarily concentrated at the corners of the column, particularly on the east and west sides. At a displacement range of 15~25 mm, the column body started to slip at the upper joint surface position, and horizontal cracks started to appear on the south and north sides. As the displacement further increased to 35~45 mm, oblique cracks on the south and north sides started to develop and gradually intersect. At 45~55 mm, the bearing capacity reached its peak point, resulting in concrete damage within the plastic hinge region (located at the base of the column with a height twice the column width) on the east and west sides. At 60~70 mm, the bearing capacity decreased to nearly 85% of the ultimate load. The concrete cover at the east and west sides within the plastic hinge range significantly spalled (Figure 7d,e, and Figure 8a). This resulted in the exposure of the longitudinal reinforcement, hoop reinforcement, and sleeves, as illustrated in Figure 8a. Furthermore, the longitudinal reinforcement exhibited flexion (Figure 8b). The column body slipped along the upper bond surface through joints, and the cracks on the south and north sides extended from the top to the bottom, reaching the neutral axis. The test specimens, in general, exhibited a damage pattern characterized by compression and bending. Importantly, the reinforcement within the sleeve was not pulled out and remained in place throughout the test, and the sleeves maintained structural integrity, as depicted in Figure 8c.

The post-cast region exhibited a rigid behavior due to its higher concrete strength compared with the column body and the presence of numerous sleeves in this region, as depicted in Figure 8d. This contributed to an augmentation in the plastic hinge's height, surpassing twice the column width. Moreover, inadequate handling during the fabrication process led to the shearing off of a segment of the hoop reinforcement located above the joint surface of the post-cast region. This resulted in inadequate confinement for the core



concrete and longitudinal reinforcement in the region. Additionally, the failure occurred due to the complete spalling of the concrete cover in the plastic hinge region, which caused a drastic decrease in the specimen's cross-sectional area of the specimen and led to a sudden and severe failure.

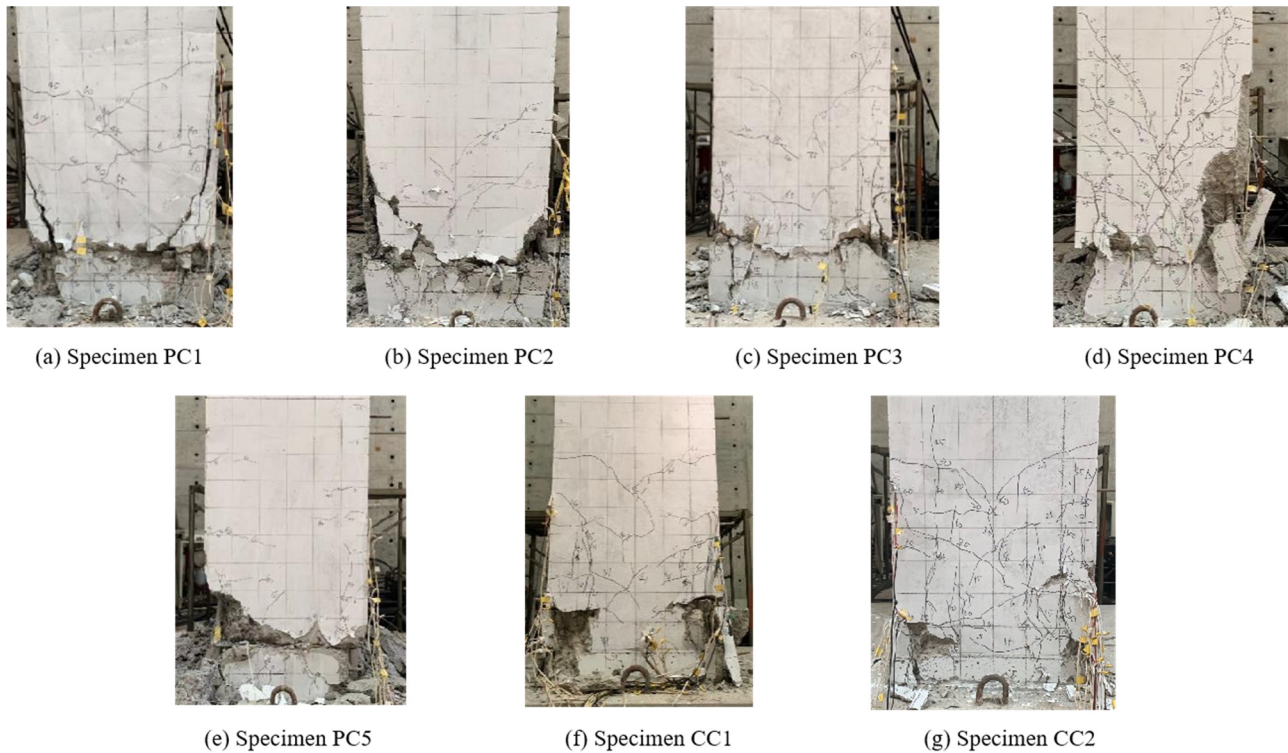


**Figure 7.** Failure patterns of specimens.

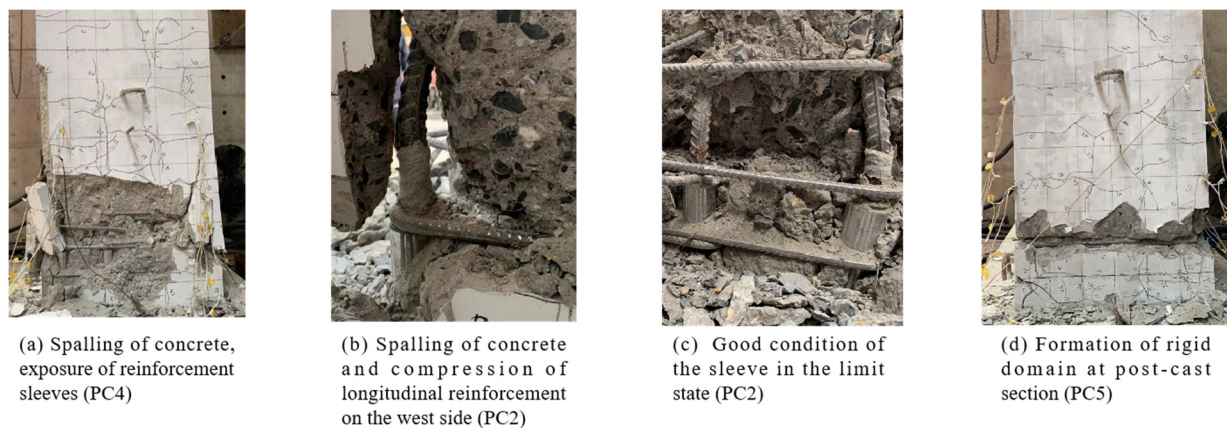


**Figure 8.** Typical failure features at specimen end.

### 3.2. Specimens CC1~CC2

When the horizontal displacement reached the range of 10~15 mm, a progressive yielding of the longitudinal reinforcement situated at the bottom of the column occurred, leading to the initiation of horizontal cracks on the tensile surface (east and west) of each specimen. With further increase in displacement, horizontal cracks also appeared on the south and north surfaces of each specimen, and there was a gradual development of horizontal cracks on the east and west surfaces. At 25~30 mm, longitudinal cracks initiated on the east and west corners of each specimen, and oblique cracks began to appear on the south and north surfaces at the same time. At this juncture, the bearing capacity reached its peak. At 35~40 mm, the corner of the column began to be damaged. The oblique cracks on

the south and north sides began intersecting, resulting in the generation of longitudinal cracks. Simultaneously, the bearing capacity of each member began to decrease. When the displacement increased to 55~60 mm, the bearing capacity of each member gradually decreased to 85% of the ultimate load, and the concrete within a 300 mm range from the base of the column exhibited ring-shaped spalling, mainly observed on the east and west sides. The corner of the column suffered severe damage, and the cracks on the south and north sides extended to the neutral axis from top to bottom. Ultimately, both specimens experienced failure in a compression–bending mode (Figure 7f,g).

#### 4. Data Result and Analysis

##### 4.1. Load–Displacement Hysteresis Curve

The relationships between the measured actuator force ( $P$ ) and the measured column top displacement ( $\Delta$ ) for all specimens are illustrated in Figure 9. Prior to the yielding of the steel, the  $P$ - $\Delta$  hysteresis curve exhibited a narrow profile, accompanied by small residual strain and low energy dissipation capacity. However, once yielding occurred, the  $P$ - $\Delta$  curve began to shift towards the displacement axis, resulting in a gradual expansion of the hysteresis loop area, thereby indicating an increased energy dissipation capacity. Furthermore, during each subsequent cycle at the same loading level, the area enclosed by the  $P$ - $\Delta$  curve experienced a slight reduction as the number of cycles increased. The hysteresis curves of the conventional cast-in-place specimens, CC1 and CC2, exhibited a distinct shuttle-shaped pattern, with CC1 demonstrating a slight pinching effect. Notably, the pinching effects were more pronounced in specimens PC1 and PC5, characterized by lower axial compression ratios compared with PC2, PC3, and PC4, which had higher ratios. These contrasting results can be attributed to the occurrence of cracks and shear slippage, specifically at the upper bond surface of the post-cast region, during testing. The results obtained from PC2 and PC3 indicate that the diameter of the longitudinal reinforcement had no influence on the shape of the hysteresis curves. Similarly, the hysteresis curves of PC3 and PC4 indicate that the stirrup spacing had no impact on their characteristics. Interestingly, there was no significant disparity observed between the hysteresis curves of PC1 and PC5. This can be attributed to the absence of shear slippage at the lower bond surface of the post-cast section, as well as the absence of dowel action in these specimens.

##### 4.2. Load–Displacement Skeleton Curve

The load–displacement relationships for all test specimens are shown by the skeleton curves in Figure 10. The ultimate load corresponded to 85% of the peak load, and the associated displacements were considered as ultimate displacements. Table 4 provides information on the yield load, peak load, ultimate load, and corresponding displacements for each specimen. The yield displacements were determined as the average values obtained using the Park method, geometric graphing method, and isoenergetic method, as detailed in Table 5.

Comparing the results of PC1 with CC1, PC5 with CC1, and PC2 with CC2, it is evident that the precast columns exhibited larger displacements at all stages in comparison to cast-in-place columns. This phenomenon can be attributed to the presence of a weaker layer at the upper bond surface of the post-cast region, contributing to the observed lower capacities in precast columns. Further comparisons between PC1 and PC2, PC5 and PC2, and CC1 and CC2 reveal that specimens with higher axial compression ratios demonstrated smaller displacements at all stages in comparison to specimens with lower ratios. Moreover, columns with higher axial compression ratios exhibited greater capacities than those with lower ratios. Analyzing PC2 and PC3 results indicates that an increase in the diameter of the longitudinal reinforcement led to gradual increases in displacements and capacities of the specimens at every stage. Examining PC3 and PC4 results reveals that a reduction in the stirrup spacing resulted in similar yield displacements and ultimate displacements for the specimens, while peak displacements decreased. This observation might be attributed

to experimental contingencies. Furthermore, decreasing the stirrup spacing resulted in a decrease in the capacity of the specimens.

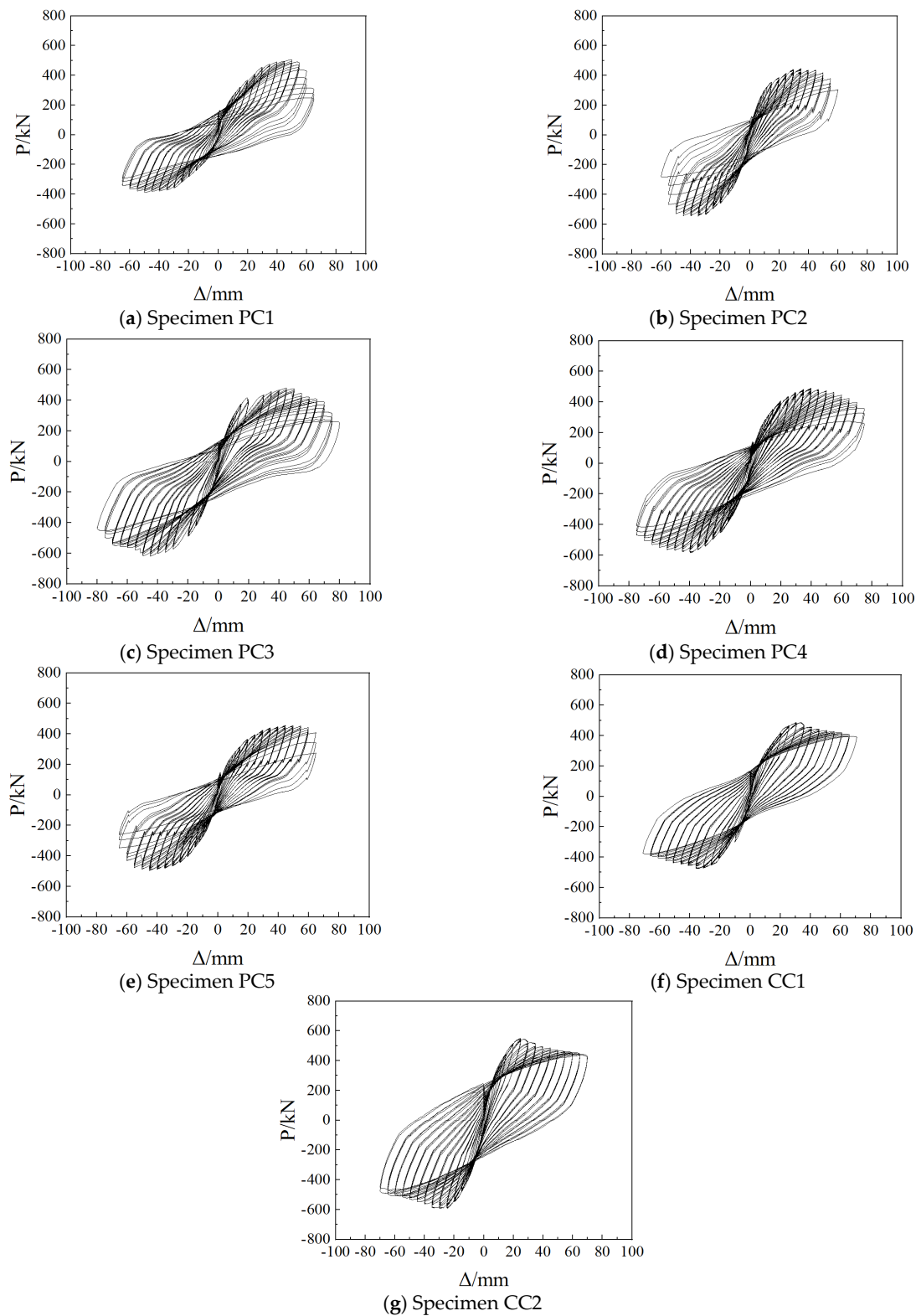


**Figure 9.** Load-displacement hysteretic loops of specimens.

Figure 10c demonstrates that for PC1, PC2, and PC5, the slopes of the skeleton curves experienced sudden changes at the ultimate stage, accompanied by a rapid decrease in

bearing capacity. This occurrence was attributed to a mistake in stirrup placement on the upper bond surface of the post-cast region during the casting process.

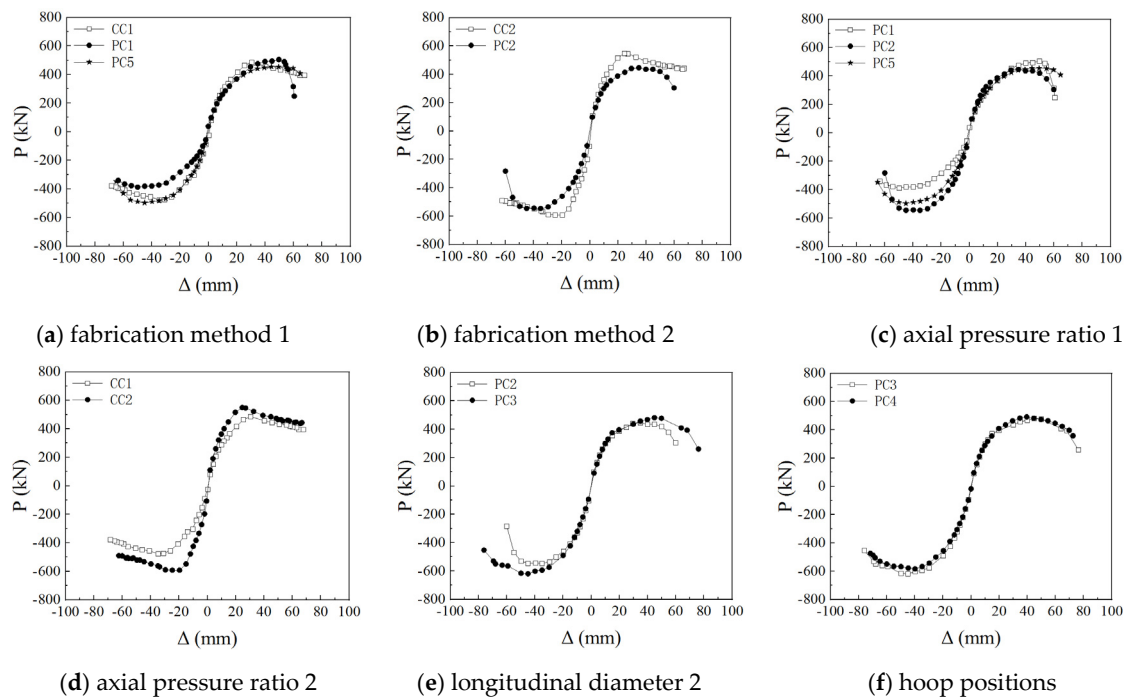


Figure 10. Load-displacement skeleton curves of specimens.

Table 4. Test results of specimens at characteristic points.

Specimen	Yield State		Peak State		Ultimate State	
	$P_y$ (kN)	$\Delta_y$ (mm)	$P_u$ (kN)	$\Delta_u$ (mm)	$P_m$ (kN)	$\Delta_m$ (mm)
PC1	367.74	25.09	446.14	49.81	379.22	60.08
PC2	406.61	17.55	496.41	34.92	421.95	54.88
PC3	460.00	21.00	550.52	44.89	467.94	66.77
PC4	443.15	21.32	537.70	39.74	457.05	67.50
PC5	394.21	21.23	476.54	44.73	405.05	62.61
CC1	399.41	19.59	481.05	32.71	408.89	59.29
CC2	488.11	16.63	570.53	27.09	484.95	55.09
Specimen	$P_{u,c}$ (kN)	$P_{u,c}/P_u$	$\theta_m = \Delta_m/l$	$\mu_\Delta = \Delta_m/\Delta_y$		
PC1	317.26	0.71	1/37	2.43		
PC2	281.66	0.57	1/41	3.19		
PC3	329.99	0.60	1/33	3.23		
PC4	334.52	0.62	1/33	3.21		
PC5	296.69	0.62	1/37	3.00		
CC1	307.44	0.64	1/38	3.05		
CC2	278.85	0.49	1/40	3.31		

Note:  $P_y$ ,  $\Delta_y$ , and  $\mu_\Delta$  represent the yield load, yield displacement, and displacement ductility coefficient, respectively.  $P_y = (P_{y1} + P_{y2} + P_{y3})/3$  denotes the average yield load obtained from three calculation methods, and  $\Delta_y = (\Delta_{y1} + \Delta_{y2} + \Delta_{y3})/3$  represents the average yield displacement derived from the three calculation methods. Similarly,  $\mu_\Delta = (\mu_{\Delta1} + \mu_{\Delta2} + \mu_{\Delta3})/3$  indicates the average displacement ductility coefficient obtained from the three calculation methods. The three calculation methods correspond to the Park method, geometric graphing method, and isoenergetic method, as detailed in Table 5.  $P_u$  and  $\Delta_u$  represent the peak load and peak displacement, respectively.  $P_m$  and  $\Delta_m$  denote the ultimate load and ultimate displacement, respectively.  $P_{u,c}$  represents the calculated value of the cross-sectional load-carrying capacity.  $\theta_m$  denotes the ultimate displacement angle, while  $l$  represents the column height. The load and displacement values in the table represent the average value for two loading directions.



**Table 5.** Indicators of specimens at yield.

Specimen	Yield Load (kN)			Yield Displacement (mm)			Ductility Coefficient		
	$P_{y1}$	$P_{y2}$	$P_{y3}$	$\Delta_{y1}$	$\Delta_{y2}$	$\Delta_{y3}$	$\mu_{\Delta1}$	$\mu_{\Delta2}$	$\mu_{\Delta3}$
PC1	392.35	334.25	376.62	28.02	21.07	26.18	2.14	2.86	2.29
PC2	418.17	383.80	417.88	18.78	15.10	18.77	2.95	3.70	2.94
PC3	469.72	444.80	465.47	21.33	18.67	23.00	3.16	3.61	2.91
PC4	457.35	418.11	453.99	22.97	18.48	22.52	2.95	3.67	3.01
PC5	409.35	368.48	404.80	23.11	18.13	22.45	2.71	3.49	2.79
CC1	418.96	375.61	403.67	21.42	17.44	19.93	2.77	3.40	2.98
CC2	494.24	483.01	487.07	17.05	16.28	16.56	3.22	3.38	3.32

Note:  $P_{y1}$ ,  $\Delta_{y1}$ , and  $\mu_{\Delta1}$  represent the yield load, yield displacement, and ductility coefficient calculated using the Park method, while  $P_{y2}$ ,  $\Delta_{y2}$ , and  $\mu_{\Delta2}$  and  $P_{y3}$ ,  $\Delta_{y3}$ , and  $\mu_{\Delta3}$  correspond to the geometric graphing method and the isoenergetic method, respectively.

#### 4.3. Energy Dissipation

The equivalent viscous damping coefficient, denoted as  $h_e$ , was utilized as a quantitative measure of energy dissipation for the first cycle at each level of cyclic loading. Table 6 presents  $h_e$  values for all specimens at different stages. The energy dissipation exhibited an ascending trend corresponding to higher amplitudes of displacement. A comparison between specimens CC2 and PC2 revealed that the  $h_e$  value for the precast column was lower than that of the entire column in the ultimate state. This disparity can be attributed to the absence of stirrups above the upper bond surface of the post-cast section region. Nevertheless, the equivalent viscous damping coefficients demonstrated similarity between the two columns in the yielding and peak states. Given the absence of the pinching effect at the bottom of the column, the parameters of specimen PC5 were similar to those of specimen PC1. Consequently, substituting the results of PC5 for PC1 is deemed reasonable, particularly when considering the abnormal  $h_e$  value of PC1. These findings are further supported by comparing CC1 with PC5. Furthermore, a comparison between the results of PC2 and PC3 indicated that the  $h_e$  values and energy dissipation of the precast columns increased proportionally with larger longitudinal reinforcement diameters. Similarly, a comparison between the results of PC3 and PC4 revealed that the  $h_e$  values and energy dissipation of the precast columns decreased as the stirrup spacing decreased.

**Table 6.** The  $h_e$  measured value of specimens.

Specimen	Equivalent Viscous Damping Coefficient		
	Yielding State	Peak State	Ultimate State
PC1	0.097	0.153	0.196
PC2	0.087	0.107	0.179
PC3	0.099	0.127	0.197
PC4	0.095	0.112	0.183
PC5	0.086	0.122	0.176
CC1	0.074	0.118	0.207
CC2	0.085	0.112	0.222

Note: The yield displacement corresponding to the equivalent viscous damping coefficient under the yield state in the table represents the average value obtained from the Park method, geometric graphing method, and isoenergetic method. The details of the yield displacement calculated by these three methods can be found in Table 5.

#### 4.4. Displacement Ductility

An examination of the experimental results presented in Tables 4 and 5 reveals notable observations regarding the displacement ductility coefficients ( $\mu$ ) and ultimate displacement angles ( $\theta$ ) of both precast and CIP columns. The  $\mu$  values of all specimens, except for PC1, reached a notable level of 3.0. Precisely, the precast columns exhibited a range of  $\mu$  values from 2.43 to 3.23, with an average value of 3.01. In contrast, the CIP columns exhibited a range from 3.05 to 3.31, averaging 3.18. Additionally, the ultimate displacement



angles ( $\theta$ ) for all specimens exceeded 1/50, with the precast columns demonstrating a range of 1/41 to 1/33, and an average of 1/36. Similarly, the CIP columns exhibited a range of 1/40 to 1/38, and an average of 1/39.

Comparing the results of PC1 with CC1, PC5 with CC1, and PC2 with CC2 revealed a close resemblance between the displacement ductility coefficients ( $\mu$ ) and ultimate displacement angles ( $\theta$ ) of precast and CIP columns, with the exception of the abnormal  $\mu$  value of PC1. Despite this, the precast columns utilizing grouted sleeves exhibited superior ductility compared with the cast-in-place columns, contrary to the experimental findings. The disparity can be attributed to the presence of numerous steel sleeves in the post-cast region, coupled with the higher concrete strength in that region, resulting in the formation of a rigid region, acting as the foundation of the column. When the specimen experienced damage, shear slippage occurred at the upper bond surface of the post-cast region. Table 4 indicates that shear slippage had minimal influence on lateral displacement during the yielding stage when the column functioned as a cohesive entity. However, as the column reached the ultimate state, shear slippage increased significantly, gradually causing the post-cast region to cease functioning in conjunction with the column body. As a consequence, the column's height decreased, resulting in increased lateral stiffness and a decrease in ultimate displacement. Further experiments and research are required to validate this conclusion, particularly regarding the impact of shear slippage on yield displacement and ultimate displacement at the upper interface of the post-cast region.

The misoperation of the stirrups on the upper bond surface of the post-cast region reduced the restraining effect on the concrete in that region. Additionally, due to the presence of the rigid region, the plastic hinge of the column shifted upward. Consequently, the concrete in the post-cast region, lacking sufficient stirrup restraint, coincided with the plastic hinge. Under repeated cyclic loading, the concrete covers in the east and west directions quickly peeled off due to inadequate stirrup restraint, resulting in a reduction in the column's cross-sectional area. This abrupt decline in capacity led to a sudden change in the slope of the skeleton curve, indicative of instantaneous damage. Furthermore, a comparison of the results of PC1 with PC2, PC5 with PC2, and CC1 with CC2 reveals that the displacement ductility coefficients ( $\mu$ ) increased with higher axial compression ratios, while ultimate displacement angles ( $\theta$ ) decreased. These contrasting observations necessitate further exploration and research to uncover the underlying reasons. The results obtained from PC2 and PC3 indicate that an increase in longitudinal reinforcement diameters enhances the displacement ductility coefficient ( $\mu$ ) and ultimate displacement angle ( $\theta$ ), thereby improving the deformation capacity of the specimens. Additionally, a comparison between PC3 and PC4 demonstrates that decreasing stirrup spacing in precast columns results in reduced values of  $\mu$  and  $\theta$ .

#### 4.5. Stiffness Degradation

The stiffness degradation curves of all specimens are illustrated in Figure 11, where the secant stiffness  $K$  is employed to characterize the stiffness degradation. The peak load and the corresponding displacement during the cyclic loading phase are denoted as  $P_i$  and  $\Delta_i$ , respectively, with  $K_i$  calculated as the ratio  $P_i / \Delta_i$ . A comparison between the results of PC2 and CC2 reveal that the precast column exhibits a lower stiffness compared with the CIP column. However, the findings from PC1 and CC1, as well as PC5 and CC1, indicate that the stiffness of the precast columns closely approximates that of the CIP columns. Consequently, further research is warranted to delve deeper into this matter. Contrastingly, comparisons involving CC1 and CC2, as well as PC1, PC2, and PC5, reveal that specimens with higher axial compression ratios exhibit higher initial stiffness yet endure a more pronounced rate of stiffness degradation. The outcomes of PC2 and PC3 suggest that specimens with larger longitudinal reinforcement diameters experience a slightly slower rate of stiffness degradation than those with smaller longitudinal reinforcement. Furthermore, the results of PC3 and PC4 indicate minimal disparities in the stiffness degradation curves concerning varying stirrup spacing. The absence of cracks and shear slippage at the lower interface of

the post-cast section region in PC5 results in design parameters that closely resemble those of PC1. Consequently, the stiffness degradation curves in the reverse loading direction for PC1 and PC5 are nearly indistinguishable. However, an anomalous behavior is observed when PC1 is subjected to loading in the forward direction.

#### 4.6. Hysteresis Curve of Reinforcement Strains

The hysteresis curves of longitudinal reinforcement strain for each specimen are shown in Figure 12. The longitudinal steel strain, denoted as  $\varepsilon$ , was obtained from strain measurement points located at both above and below the sleeves. In the initial loading phase, the hysteresis curves of steel strain exhibited a narrow and slender profiles. The residual strains remained minimal, and the curves exhibited a gradual change in the slope. As loading displacement increased and steel yielded, the slope of the curves progressively decreased, accompanied by an increase in residual strains. At the onset of loading, the strain curve above the sleeves closely resembled the corresponding curve below the sleeves. However, post-yielding, a noticeable divergence between these two curves emerged, with the gap progressively widening. Except for PC3, all specimens reached a state of yielding in the longitudinal steel strains measured above the sleeves upon reaching the peak load, indicative of a plastic hinge region development above the sleeves. In the ultimate state, both longitudinal steel strains above and below the sleeves exhibited yielding behavior.

#### 4.7. Ultimate Capacity

Based on the preceding analysis, it was observed that the longitudinal reinforcements located above the upper bond surface of the post-cast region yielded first upon reaching the ultimate state, followed by concrete crushing, indicative of the characteristic behavior associated with large-eccentricity columns. In accordance with the Code for Design of Reinforced Concrete Structures (GB50010-2010), Table 4 presents the test values and theoretical calculated values of the ultimate capacity for each specimen, all considered as large-eccentricity columns. For all specimens, the test values of ultimate capacity ( $P_u$ ) exceeded the corresponding theoretical calculated values ( $P_{u,c}$ ), with the average ratio of  $P_{u,c}/P_u$  across all specimens being 0.61. Specifically, the average ratio of  $P_{u,c}/P_u$  for precast columns was 0.62, while that for cast-in-place columns was 0.56. Moreover, the ratio of  $P_{u,c}/P_u$  for columns with an axial compression ratio of 0.25 was 0.66, whereas for columns with an axial compression ratio of 0.40, it was 0.57. These findings indicate that the calculated compression–bending ultimate capacity of the positive section region, as per GB50010-2010, considering negligible contributions from sleeves and stirrups, exhibited a certain level of safety. Upon comparing PC1 and CC1, PC5 and CC1, PC2 and CC2, it is evident that the maximum capacity of the precast column is smaller than that of the cast-in-place column due to the presence of a weak layer at the interface in the post-cast section region. In comparing PC1 and PC2, PC5 and PC2, CC1 and CC2, it can be observed that the maximum capacity gradually increases with an increase in axial compression ratios. However, the calculated values exhibit the opposite trend, as the column transitions to a small-eccentricity column at high axial compression ratios, resulting in a decrease in the calculated maximum capacity. Furthermore, a comparison between PC2 and PC3 demonstrates that the maximum capacity of the columns increases with an increase in longitudinal reinforcement diameter. Conversely, based on the results of PC3 and PC4, it is evident that the maximum capacity decreases with a decrease in stirrup spacing.

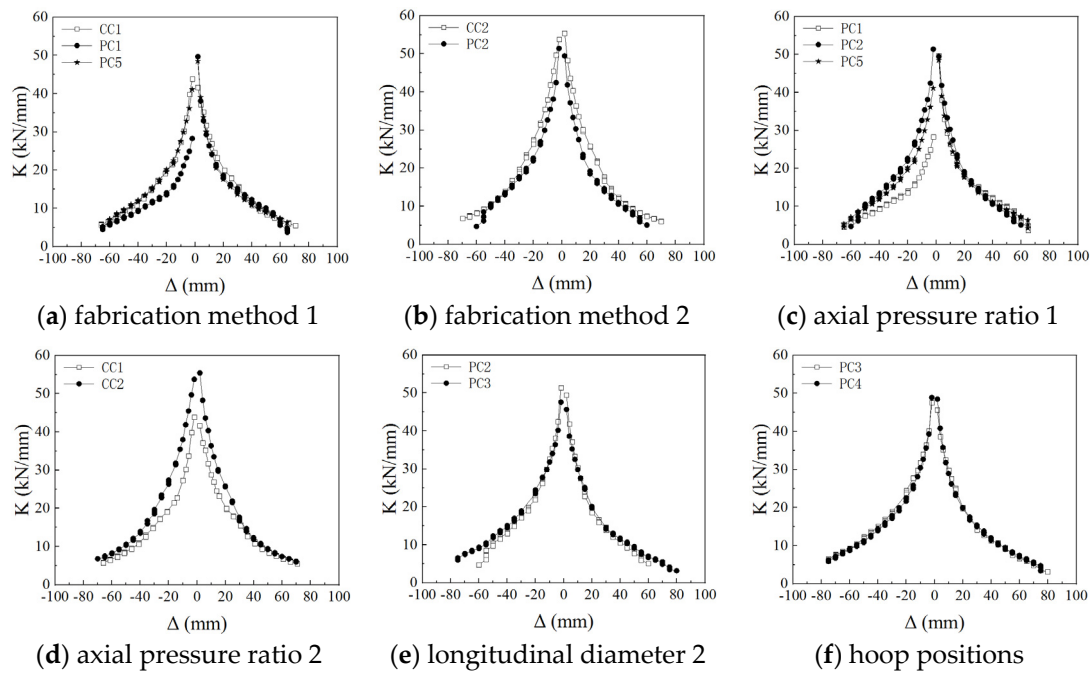


Figure 11. Stiffness degradation curves of specimens.

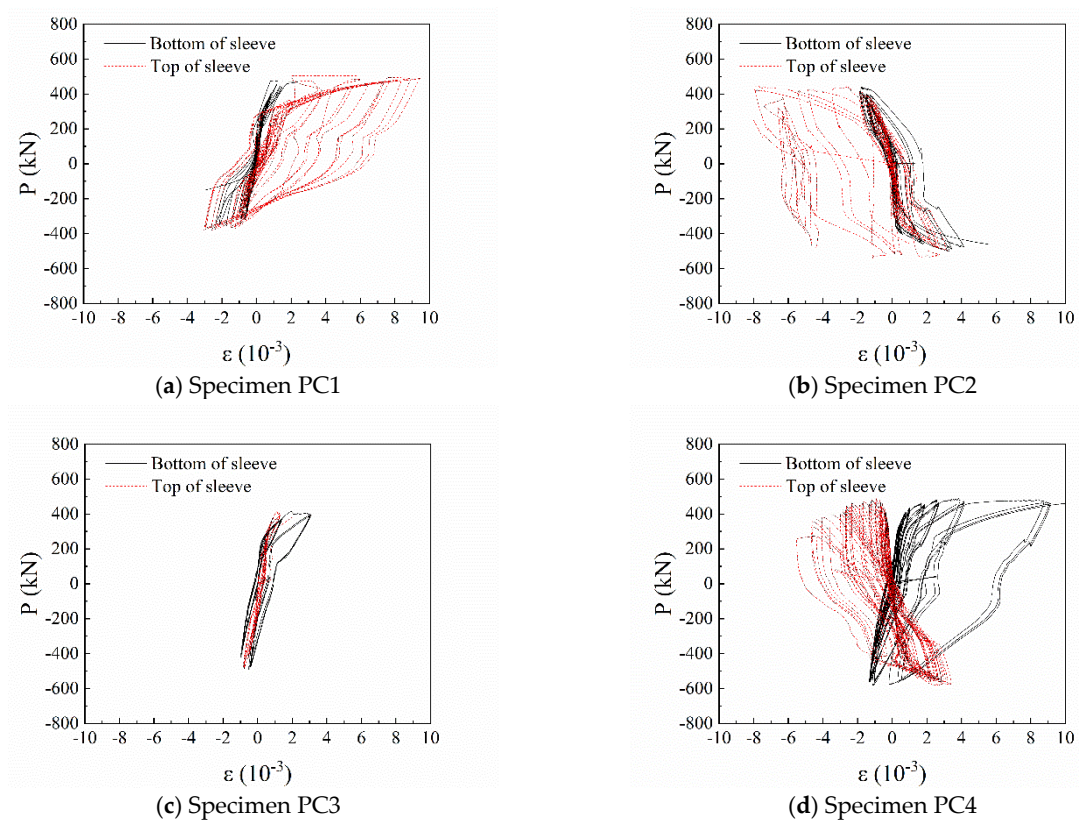
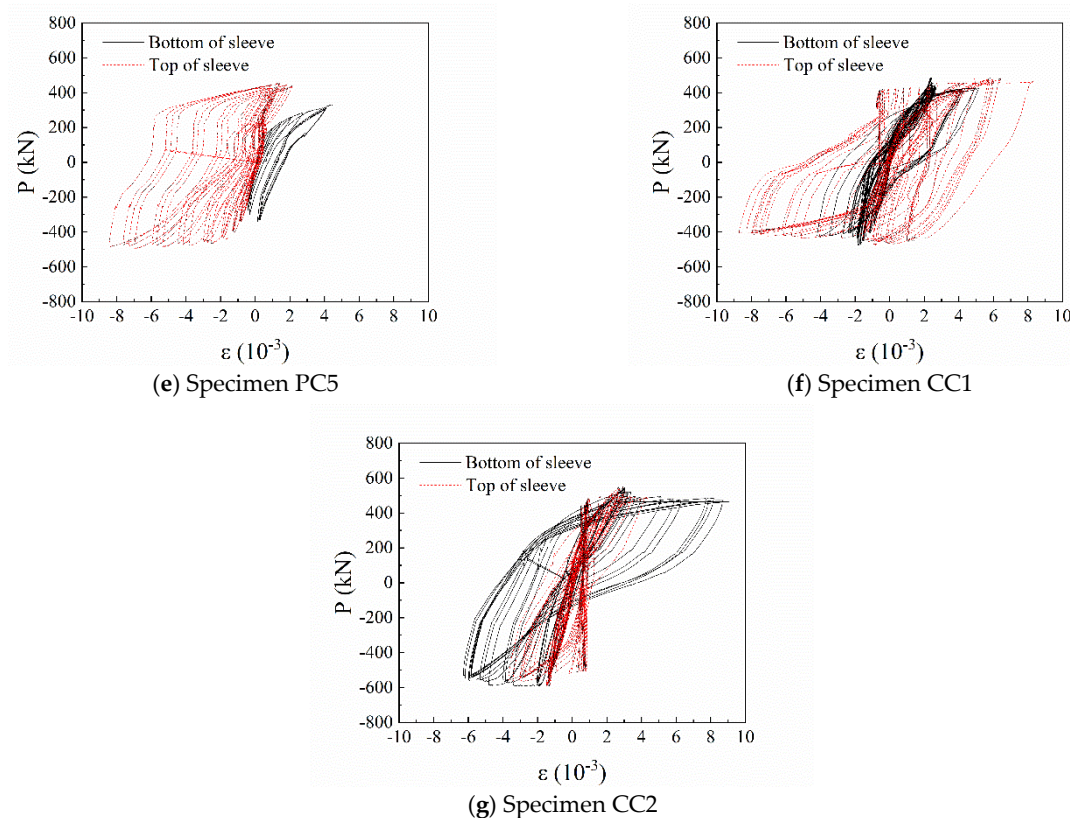


Figure 12. Cont.



**Figure 12.** Hysteresis loops for strains of longitudinal reinforcements.

## 5. Conclusions

The comprehensive evaluation of this study, considering potential concrete unevenness during casting, casting challenges at nodal points, imperfect verticality alignment between precast columns and bases, and local stirrup mispositioning, yields several noteworthy findings that can be drawn as follows:

1. The specimens exhibited large eccentric compression failure at the upper bond surface of the post-cast region, representing the ultimate limit state. The average ratio between the calculated values based on GB50010-2010 and the test values of the capacity for each precast specimen was 0.62, indicating a high level of safety. The ultimate displacement angle of the precast specimens satisfied the ultimate elastic–plastic story drift requirement set in GB50011-2010 (1/50), with a range of 1/37 to 1/41. The specimens achieved the “no collapse under large earthquake” criteria, and the sleeves remained intact without any pullout or breakage, with no observable vertical or lateral cracking. Overall, the novel dry sleeve connection effectively transferred the tension and pressure of the reinforcement, making it suitable for longitudinal reinforcement connections in prefabricated reinforced concrete frames.
2. The precast specimens exhibited slightly lower ultimate capacity, displacement ductility, and energy dissipation in the ultimate state compared with the cast-in-place specimens. However, they demonstrated higher energy dissipation in the yield state and peak state.
3. Precast columns with smaller axial compression ratios experienced cracking and shear slippage at the upper bond surface of the post-cast section region, resulting in pinching hysteresis curves. In contrast, precast columns with larger axial compression ratios exhibited relatively complete hysteresis curves. As the axial compression ratio increased, the capacity in each state, ductility, and energy dissipation of the precast columns improved, while the displacements in each state decreased.



4. Increasing the longitudinal reinforcement diameter resulted in higher capacities and displacements in each state for the precast columns.
5. Decreasing the stirrup ratio resulted in reduced capacities of precast columns in each state, accompanied by increased displacements in yielding and ultimate states.
6. The post-cast region formed a rigid region causing predominant damage at and above the bond surface of the post-cast section. Stirrup failure above the upper bond surface of the post-cast region resulted in accelerated peeling of the concrete cover, followed by rapid crushing of the core concrete. This abrupt damage suggests potential avenues for further improvement in seismic performance. The integrity of the post-placement area can be improved by raising the concrete mark, setting the gear contact surface, and optimizing the placement scheme, such as increasing the formwork depth of the placement opening or using self-compacting concrete.

In the future research, the adaptability of the novel dry sleeve in various assembled structural members (such as shear wall, beam, multi-member joints, etc.) will be further studied. Secondly, in order to capture the dynamic and complex load conditions experienced in international seismic events, it is necessary to consider the seismic performance of prefabricated components under dynamic load scenarios in further research to enhance the applicability of the study to actual seismic conditions. Finally, it is also necessary to clearly address the impact of potential external factors (such as material properties, construction quality or changes in environmental conditions, etc.) on the actual performance of novel dry sleeve connections.

**Author Contributions:** Methodology, H.W.; Validation, B.Z.; Investigation, X.H., A.D. and D.Z.; Data curation, X.H.; Writing—original draft preparation, X.H., H.W. and D.Z.; Writing—review & editing, H.W., A.D., B.Z. and D.Z. All authors have read and agreed to the published version of the manuscript.

**Funding:** This research received no external funding.

**Data Availability Statement:** Data are contained within the article.

**Conflicts of Interest:** Author Baojun Zhao was employed by the company China State Construction Hailong Technology Co., Ltd. Author Dekai Zhang was employed by the company China Construction Eighth Engineering Division Corp., Ltd. The remaining authors declare that the research was conducted in the absence of any commercial or financial relationships that could be construed as a potential conflict of interest.

## References

1. Liu, D.; Gambatese, J. Construction worker and equipment energy consumption for offsite precast concrete. *Pract. Period. Struct. Des. Constr.* **2020**, *25*, 04020007. [CrossRef]
2. Ou, Z.J.; Chen, W.L.; Cao, L. Seismic performance investigation of UHPC precast concrete composite columns. *J. Southwest Jiaotong Univ.* **2024**, 1–9. Available online: <http://kns.cnki.net/kcms/detail/51.1277.U.20230707.1614.006.html> (accessed on 11 January 2024). (In Chinese).
3. Xu, L.; Pan, J.L.; Cai, J.M. Seismic performance of precast RC and RC/ECC composite columns with grouted sleeve connections. *Eng. Struct.* **2019**, *188*, 104–110. [CrossRef]
4. Paudel, S.; Tanapornraweevit, G.; Tangtermsirikul, S. Numerical investigation of concrete filled hollow precast composite columns subjected to lateral cyclic loading. *Eng. Struct.* **2022**, *252*, 113586. [CrossRef]
5. Ahmed, S.; Arocho, I. Feasibility assessment of mass timber as a mainstream building material in the US construction industry: Level of involvement, existing challenges, and recommendations. *Pract. Period. Struct. Des. Constr.* **2021**, *26*, 04021008. [CrossRef]
6. Lallas, Z.N.; Gombada, M.J.; Mendonca, F. Review of supplementary cementitious materials with implications for age-dependent concrete properties affecting precast concrete production. *PCI J.* **2024**, *68*, 46–64.
7. Dolati, S.S.K.; Mehrabi, A. NSM FRP pile-splice system for prestressed precast concrete piles. *Pract. Period. Struct. Des. Constr.* **2022**, *27*, 04022046. [CrossRef]
8. Longinow, A.; Mohammadi, J. Effects of vibrations on structures: Overview and case studies. *Pract. Period. Struct. Des. Constr.* **2022**, *27*, 04022049. [CrossRef]
9. Stanikzai, M.H.; Elias, S.; Chae, Y. Recent advances in hybrid vibration-control Systems. *Pract. Period. Struct. Des. Constr.* **2022**, *27*, 03122003. [CrossRef]



10. Arockiasamy, M.; Arvan, P.A. Behavior, performance, and evaluation of prestressed concrete/steel pipe/steel H-pile to pile cap connections. *Pract. Period. Struct. Des. Constr.* **2022**, *27*, 03122001. [[CrossRef](#)]
11. Sun, C.; Zhuang, M.L.; Bai, L.; Gao, L.; Yu, C.; Yang, J.; Zhu, H.; Qiao, Y.; Shao, Y.; Zhang, W. Experimental study on seismic performance of novel precast concrete beam-column joints using mechanical connections. *Bull. Earthq. Eng.* **2023**, *21*, 4429–4448. [[CrossRef](#)]
12. Gao, P.N.; Deng, Y.; Li, A.Q.; Lu, F.Y. Review on seismic performance of connection joints of prefabricated concrete frame structures. *Ind. Constr.* **2021**, *51*, 171–185+152. (In Chinese)
13. Shemshadian, M.E.; Schultz, A.E.; Le, J.-L.; Labbane, R.; Laefer, D.F.; Al-Sabah, S.; Truong-Hong, L.; Huynh, M.P.; McGetrick, P.; Martin, T.; et al. AMASS: Advanced manufacturing for the assembly of structural steel. *Pract. Period. Struct. Des. Constr.* **2021**, *26*, 04020052. [[CrossRef](#)]
14. Hu, X.; Zeng, L.; Wu, H.; Djerrad, A.; Yang, C.; Zhang, D. Experimental study on crack width of HRB600 grade high-strength steel bar reinforced concrete beams. *Buildings* **2024**, *14*, 10. [[CrossRef](#)]
15. Chourasia, A.; Singhal, S.; Manivannan. Prefabricated volumetric modular construction: A review on current systems, challenges, and future prospects. *Pract. Period. Struct. Des. Constr.* **2023**, *28*, 03122009. [[CrossRef](#)]
16. Ong, H.Y. Experimental Study of Grout Filled Splice Sleeve Integrated with Shear Key for Precast Concrete Connection. Ph.D. Thesis, Technological University of Malaysia, Johor, Malaysia, 2010.
17. Ogura, K. *Testing Program for the NMB Splice Sleeve*; Splice Sleeve North America, Inc.: Birmingham, MI, USA, 2005.
18. Zhang, X.H.; Wang, J.; Pan, S.B.; Jiang, W.S.; Li, Q.N.; Yu, Q.R. *Experimental Research on Seismic Performance of New Fabricated Column Spliced by Grout Sleeves*; Natural Science Edition; Xi'an University of Architecture and Technology: Xi'an, China, 2013; Volume 45, pp. 164–170. (In Chinese)
19. Ameli, M.J.; Parks, J.E.; Brown, D.N.; Pantelides, C.P. Seismic evaluation of grouted splice sleeve connections for reinforced precast concrete column-to-cap beam joints in accelerated bridge construction. *PCI J.* **2015**, *60*, 80–1030. [[CrossRef](#)]
20. Zhang, Z. *Seismic Performance Research of Precast Concrete Columns in High-Rise Buildings*; Harbin Institute of Technology: Harbin, China, 2013. (In Chinese)
21. Kim, Y. *A Study of Pipe Splice Sleeves for Use in Precast Beam-Column Connections*; University of Texas at Austin: Austin, TX, USA, 2000.
22. Riva, P. Seismic behavior of precast column-to-foundation grouted sleeve connections. In Proceedings of the International Conference on Advances in Engineering Structures, Mechanics & Construction, Waterloo, ON, Canada, 14–17 May 2006; pp. 121–128.
23. Xiangmin, L.; Rundong, G.; Qingfeng, X. Experimental study on influence of grouting defect on joint strength of grout sleeve splicing of rebars. *Build. Struct.* **2018**, *48*, 52–56. (In Chinese)
24. Zhang, W.J.; Guo, Y.Y.; Liu, S.W. Experimental research on seismic behavior of precast RC columns with steel bars spliced by compressive sleeves. *Eng. Mech.* **2016**, *33*, 119–127. (In Chinese)
25. Chen, Q.J.; Pan, Z.Y.; Cai, J.; Liang, J.J.; Zhu, D.F.; Chen, Q.R. Experimental research on seismic behaviors of assembled beam-column joints with rebars spliced by pressed sleeves. *J. Southeast Univ.* **2019**, *49*, 918–925.
26. Pengfei, L.; Xuehui, A.; Shiqin, H.; Chen, C. Mathematical model for dowel bearing capacity considering the effect of concrete damage. *J. Tsinghua Univ.* **2016**, *56*, 1255–1263. (In Chinese)
27. Wang, X.F. Study on Seismic Behavior of Concrete Frame Columns with High-Yield-Strength Reinforcements. Ph.D. Thesis, China Academy of Building Research, Beijing, China, 2013. (In Chinese).
28. GB 50011-2010; Code for Seismic Design of Buildings. China Architecture & Building Press: Beijing, China, 2010.

**Disclaimer/Publisher's Note:** The statements, opinions and data contained in all publications are solely those of the individual author(s) and contributor(s) and not of MDPI and/or the editor(s). MDPI and/or the editor(s) disclaim responsibility for any injury to people or property resulting from any ideas, methods, instructions or products referred to in the content.